PCCP

PAPER

View Article Online
View Journal | View Issue

Cite this: *Phys. Chem. Chem. Phys.*, 2026, **28**, 871

A theoretical investigation on the mechanistic and kinetic study of 2,2,3,3,4,4,5,5-octafluorocyclopentanol with OH radicals and Cl atoms and its implications in new particle formation

Suresh Tiwari and Ranga Subramanian *

Fluorinated alcohols are used in various industrial applications, including coatings, paints, adhesives, polymers, waxes, and polishes, as well as for cleaning electronic components. Consequently, the presence of fluorine atoms in these compounds contributes to their atmospheric persistence, allowing them to act as potent greenhouse gases, even at trace concentrations. The potential risks and hazards of novel chemical substances were assessed before they were introduced into society. Therefore, a key component of atmospheric chemistry in our study is the oxidation of 2,2,3,3,4,4,5,5-octafluorocyclopentanol (cyc-$(CF_2)_4$CHOH–) by hydroxyl (OH) radicals and chlorine (Cl) atoms, as well as how this molecule participates in new particle formation (NPF) in the atmosphere, studied through molecular dynamics (MD) simulations. All reaction energetics and thermodynamic parameters were calculated utilizing the M06-2X/6-311+G(2d,2p) and MP2/6-311+G(2d,2p) methodologies. The resulting optimized geometries were then employed for single-point energy calculations at the CCSD(T) level using cc-pVXZ (D and T) basis sets. Complete basis set (CBS) extrapolation was performed to obtain accurate rate coefficient calculations. Four hydrogen atom abstraction channels are feasible for the aforementioned title reactions. Possible H-abstraction reaction pathways were identified for these atmospheric oxidising agents, and the rate coefficients were evaluated over the 220–420 K temperature range. The atmospheric implications of the cyc-$(CF_2)_4$CHOH– compound were computed based on its rate coefficient values, and its atmospheric fate and implications are discussed.

Received 10th July 2025,
Accepted 19th November 2025

DOI: 10.1039/d5cp02637g

rsc.li/pccp

1. Introduction

Chlorofluorocarbons (CFCs), hydrochlorofluorocarbons (HCFCs), and hydrofluorocarbons (HFCs) have been widely employed in various industries over the last several decades.[1–3] The Kyoto Protocol (1997)[4] and Montreal Protocol (1987)[5,6] prohibit the use of ozone-depleting substances to restore stratospheric ozone. These substances have prompted the search for more sustainable and ecologically friendly replacements, owing to their significant potential for global warming and ozone depletion. These substitutes should meet industrial and commercial demands while having minimal effects on ozone depletion and climate change.[7] A family of compounds called fluorinated alcohols is being explored as potential replacements for CFCs due to their high chemical reactivity and ability to cause zero ozone depletion.[8,9] Fluorinated alcohols have replaced CFCs in various applications, including carrier compounds for lubricants, cleaning of electronic components, and refrigeration.[10] However, because of the presence of the C–F bond in fluorinated alcohols, these chemicals absorb infrared radiation inside the atmospheric window (8 to 12 μm), contributing to rising atmospheric temperatures.[11] During the daytime, oxygenated volatile organic compounds (OVOCs) mainly degrade in the troposphere *via* OH radicals. The OH radical is a highly reactive atmospheric oxidant that easily reacts with various nearby species, including radical scavengers and organic pollutants, through immediate, non-selective reactions.[12] That is why this radical is known as the ''detergent of the atmosphere'' or ''tropospheric vacuum cleaner.'' In the past few years, the oxidation process involving chlorine atoms has gained significant importance in atmospheric reactions, particularly for its influence on the boundary layer of marine and coastal regions and the Arctic troposphere during the spring season.[13] Thus, it is crucial to know the kinetic parameters of their reactions with OH radicals and Cl atoms to determine how OVOCs affect the air quality index in contaminated areas.[14]

Department of Chemistry, Indian Institute of Technology Patna, 801103, India. E-mail: ranga@iitp.ac.in

OVOCs also lead to the creation of new particles (NPF), which are a significant factor in the accumulation of secondary organic aerosols (SOAs) in the atmosphere and affect weather, climate, air quality, and human health.[15] This has been observed in various locations, including the troposphere, coastal and metropolitan areas, and boreal forests.[16,17] Although NPF is important, not enough is known about the basic molecular processes behind it.[18] Prior research has shown that the essential substances, water, and sulfuric acid (SA) drive the early stages of atmospheric particle creation; nevertheless, their condensation only allows for an insignificant amount of the development of atmospheric nanoparticles.[19–21] Therefore, a more thorough understanding of organic-driven nucleation mechanisms is necessary to elucidate their atmospheric importance.

2,2,3,3,4,4,5,5-Octafluorocyclopentanol, also known as cyc-$(CF_2)_4$CHOH–, is a novel fluorinated cyclic alcohol used as a CFC substitute in semiconductor cleaning agents.[22] To the best of our knowledge, only one study has reported on the tropospheric gas-phase reaction with OH radicals, and it explored this reaction using quasi-theoretically obtained rate constants. Their computed rate coefficient with the OH radical is 6.5×10^{-14} cm^3 molecule^{-1} s^{-1} at 296 K.[23] The GWP for cyc-$(CF_2)_4$CHOH– on a 100-year time horizon was determined by adjusting the instantaneous radiative efficiency with its atmospheric lifetime, yielding a value of 13. The experimentally obtained integrated absorption cross-section was 21.1×10^{-17} cm^2 molecule^{-1} cm^{-1}.[24] Prior research on the kinetics of the Cl atom is not accessible. To the best of our knowledge, the degradation of cyc-$(CF_2)_4$CHOH– by OH radicals and Cl atoms has not yet been thoroughly studied theoretically, especially in terms of their role in new particle formation (NPF). Therefore, the reaction pathways, kinetics, intermediate products, and NPF were also investigated. We employed high-level *ab initio* and density functional theory (DFT) approaches for tropospheric kinetic research using OH radicals and Cl atoms. Multiple reaction pathways are possible for the cyc-$(CF_2)_4$CHOH– compound, hydrogen atom abstracted from the methine (C–H) and hydroxyl (O–H) positions, as shown in Scheme 1. Furthermore, we examined the thermodynamic characteristics of fluorine abstraction in the presence of Cl and OH radicals. The kinetics of the fluorine abstraction were not examined. Indeed, these reactions are unfavorable because of their highly positive $(\Delta H^{\circ}_{298.15})$ and Gibbs free energy $(\Delta G^{\circ}_{298.15})$ values.

Therefore, we investigated the kinetics of hydrogen abstraction using Cl atoms and OH radicals over the 220–420 K temperature range. This information will be helpful for simulating atmospheric kinetics and other practical applications. We have studied NPF through classical mechanics-based molecular dynamics simulations. The atmospheric implication parameter for cyc-$(CF_2)_4$CHOH– compounds is calculated based on the computed rate coefficients. Because of the existence of C–F bonds, atmospheric implication calculations were used to determine the possible climate forcing effect of the compound. Additionally, we computed the dielectric strength (DS) value as a substitute for SF_6, which is a crucial greenhouse gas. We also investigated the dissociative pathway mechanisms of secondary

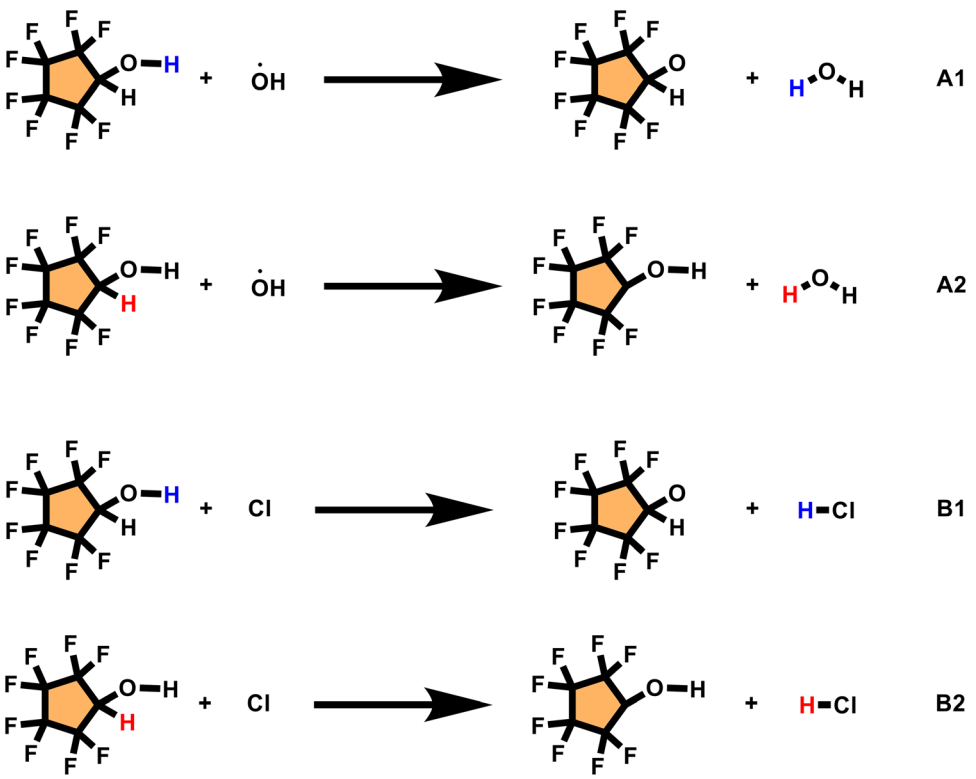

Scheme 1 A mechanistic depiction of the abstraction of hydrogen atoms by OH radicals and Cl atoms.

radicals to study their atmospheric fates, parent molecule toxicity, and degradation products.

2. Computational techniques

2.1 Electronic structure calculation

All stationary points that are part of the hydrogen abstraction in the reaction channel, reactant (cyc-$(CF_2)_4$CHOH–), reactant complexes (RCs), transition states (TSs), product complexes (PCs), and products were optimized and frequency calculations were performed using the *ab initio* MP2[25] and DFT-based M06-2X[26–28] methods with the Pople 6-311+G(2d,2p) basis set.[26,29–33] In several investigations, this hybrid density functional (M06-2X) has been employed to examine kinetic parameters, barrier heights, hydrogen bonding interactions, and reaction processes for a range of atmospherically significant reactions.[34,35] Vibrational frequency calculations verified the transition-state concepts and stable minima of the potential energy surface (PES). Real frequencies were used to characterize all local minima, and the existence of one imaginary frequency confirmed the transition states. To validate the proposed reaction routes, intrinsic reaction coordinate (IRC)[36,37] computations were performed at the M06-2X/6-311+G(2d,2p) level to verify that each transition state connects the proposed reactants and products (see Fig. S5). To avoid spin contamination, all reactive species were assessed before and after annihilation, as contamination may result in inaccurate barrier heights. For the titled reactions, spin contamination is not a concern at the M06-2X/6-311+G(2d,2p) level with OH radicals and Cl atoms, as verified by the $\langle S^2 \rangle$ values tabulated in Table S3. The GaussView program is used to visualize optimized geometry, IRC pathways, and normal mode vibrational frequencies.[38]

As a result, utilizing the M06-2X/6-311+G(2d,2p) optimized geometries, we performed single-point energy calculations using the high-level coupled-cluster single-double and perturbative triples (CCSD(T))[39] technique with a cc-pVXZ[40] (X = D and T) basis set to refine the potential energy surface and obtain more accurate energy. In order to further improve the accuracy of the electronic energies, we extrapolate them to the complete basis set (CBS) limit using the CCSD(T) with cc-pVXZ basis sets (where X = 2 and 3) in conjunction with corrected energies from the MP2 method with cc-pVXZ (X = 2, 3, and 4) basis sets, as follows, and CBS extrapolation denoted as CCSD(T)-MP2/CBS, which is shown below:[41]

$$\begin{aligned} E_{\text{CCSD(T)-MP2/CBS}} &= E_{\text{CCSD(T)/TZ}} + \left(E_{\text{CCSD(T)/TZ}} - E_{\text{CCSD(T)/DZ}}\right) \\ &\times \frac{3^4}{4^4 - 3^4} + E_{\text{MP2/QZ}} + \left(E_{\text{MP2/QZ}} - E_{\text{MP2/TZ}}\right) \\ &\times \frac{4^4}{5^4 - 4^4} - E_{\text{MP2/TZ}} - \left(E_{\text{MP2/TZ}} - E_{\text{MP2/DZ}}\right) \\ &\times \frac{3^4}{4^4 - 3^4} \end{aligned} \tag{1}$$

Here, DZ, TZ, and QZ represent the cc-pVDZ, cc-pVTZ, and cc-pVQZ basis sets, respectively.

Furthermore, the T1 diagnostic values computed at the CCSD(T)/cc-pVXZ level of theory[42,43] (X = D and T) are tabulated in Table S4. The zero-point energy (ZPE) was scaled by a factor of (0.971),[44] and the spin–orbit coupling (SOC)[45] correction was included in the $E_{\text{CCSD(T)-MP2/CBS}}$ energies to obtain more accurate energies for all reactive species. The computed T1 values ranged from 0.012 to 0.032, which is less than the threshold value of 0.045 for open-shell species. Consequently, there was no problem with the multireference character of the CCSD(T) wavefunction. These T1 values support the CCSD(T) single-reference method for determining the barrier heights of various reactions and other kinetic computations.

2.2 Molecular dynamics (MD) simulation

The GROMACS 2024 simulation software with the AMBER general force field (GAFF), which has been extensively used in atmospheric molecular simulations, was used to perform classical molecular dynamics simulations to examine the nucleation process of cyc-$(CF_2)_4$CHOH– clusters.[46,47] The ESP charges were obtained at the M06-2X/6-311+G(2d,2p) level of theory. Restrained electrostatic potential (RESP) charges were fitted with Antechamber (AmberTools), and the relevant Amber parameters and coordinate files were generated utilizing Sleap. Then, the AnteChamber Python Praser interface (ACPYPE) was used to generate GROMACS files.[48] Subsequently, cyc-$(CF_2)_4$CHOH–, sulfuric acid (SA), nitrogen (N_2), and oxygen (O_2) were among the molecules placed at random into the 200 × 200 × 200 Å^3 simulation box. A 1 ns NVT equilibration was performed at 298 K after energy minimization, and then a 40 ns simulation was run in the NPT ensemble at 298 K and 1 bar. A velocity-rescaling[49] thermostat was used to establish temperature coupling, and a C-rescaling[50] barostat was used to maintain the pressure control. An integration time step of 1 femtosecond was applied. The particle-mesh Ewald (PME) approach was employed for evaluating long-range electrostatics, whereas van der Waals and electrostatic interactions were approached with a cutoff distance of 1.4 nm.[51] The LINCS method was used to deal with bond constraints.[52]

3. Results and discussion

3.1 Electronic structures of stationary points

All the optimized geometries of the stationary points (R = (cyc-$(CF_2)_4$CHOH–), RCs, TSs, PCs, and Ps) involved in each reaction route of the titled reactions are displayed in Fig. S1. The bond lengths and angles for these stationary points were obtained at the M06-2X/6-311+G(2d,2p) and MP2/6-311+G(2d,2p) theoretical levels. Fig. S1 shows that the optimized geometric parameters at both theoretical levels were in good agreement. Vibrational frequencies were also computed using M06-2X/6-311+G(2d,2p) and MP2/6-311+G(2d,2p) theoretical levels. The vibrational frequency values with limited experimental data are listed in Table S1. The stretching modes of the coupling breakdown and bond formation correspond to one imaginary frequency in each transition state, and the imaginary frequencies calculated for TSA1, TSA2, TSB1, and TSB2 at the M06-2X/6-

311+G(2d,2p) level of theory are 1843.28*i*, 1015.31*i*, 1436.84*i*, and 897.09*i* cm^{-1}, respectively. There are four possible hydrogen abstraction channels for the reaction of cyc-$(CF_2)_4$CHOH– with OH radicals and Cl atoms: hydrogen abstraction from the hydroxyl (O–H) position and hydrogen abstraction from the methyne (C–H) group. Analogous to hydrogen abstraction, fluorine atoms can also be abstracted from the cyc-$(CF_2)_4$CHOH– compound using OH radicals and Cl atoms, as shown in the SI (Scheme S1). The computed reaction enthalpy $(\Delta H^{\circ}_{298.15})$ and Gibbs free energy $(\Delta G^{\circ}_{298.15})$ values were both highly positive for fluorine atom abstraction, as shown in Table 1. Hence, these pathways are both thermodynamically unfavorable and insignificant under atmospheric conditions; therefore, they were not considered further in the rate coefficient calculations. This led us to concentrate on the kinetics of hydrogen abstraction, and our calculations revealed that the hydrogen abstraction reaction pathways contained four transition states: TSA1, TSA2, TSB1, and TSB2. We found that the dissociating O–H bonds in TSA1 and TSB1 were 14.41% and 25.19% longer than the equilibrium O–H bond distance in cyc-$(CF_2)_4$CHOH–, respectively. The dissociating C–H distance increased by 7.46% and 14.50% relative to the equilibrium C–H bond distance in cyc-$(CF_2)_4$CHOH– (TSA2 and TSB2), respectively. The H–O (TSA1 and TSA2) and H–Cl (TSB1 and TSB2) bonds were stretched by 18.9%, 30.17%, 9.70%, and 25.19%, respectively, compared with the equilibrium H–O and H–Cl bond distances in the free H_2O and HCl molecules. From the transition states TSA1, TSA2, TSB1, and TSB2, it is clear that the elongation of forming bonds is greater than that of dissociating bonds in the case of TSA1, TSA2, and TSB2 transition states. However, in the case of the TSB1 transition state, we found that the broken bond (O–H) elongates significantly more than the forming bond (H–Cl). Therefore, according to Hammond's postulate,[53] these transition states, TSA1, TSA2, and TSB2, are reactant-like, and the reactions proceed *via* an early transition state, as expected for exothermic reactions (Table 1). The reaction enthalpies $(\Delta H^{\circ}_{298.15})$ are negative, and in the case of TSB1, they are product-like, and the reaction proceeds *via* a late transition state, as expected. The reaction enthalpies $(\Delta H^{\circ}_{298.15})$ were positive, and the reaction pathways were endothermic.

3.2 Reaction energetics

The potential energy surface (PES) for the reaction of cyc-$(CF_2)_4$CHOH– with OH radicals and Cl atoms was constructed at the CBS level using CCSD(T)-MP2 extrapolation. For ease of presentation, the relative energies, including scaled ZPE and SOC corrections (ΔE + ZPE + SOC) in kcal mol^{-1}, are related to the reactants, which are set to zero. All relative energies are provided in the SI (Table S2). Pre-reactive (RCA1, RCA2, RCB1, and RCB2) and post-reactive (PCA1, PCA2, PCB1, and PCB2) complexes were retained *via* non-covalent interactions (NCI) among O, H, and Cl atoms in the reaction channels A1, A2, B1, and B2. Their description utilizing bond lengths, NCI isosurfaces, and AIM topological analysis (Fig. S1, S2, and S4) validated the PES shown in Fig. 1.

3.2.1 Hydrogen abstraction *via* OH radicals. When the OH radical approaches the hydroxyl hydrogen (O–H) of cyc-$(CF_2)_4$CHOH– in reaction channel A1, firstly, a reactant complex (RCA1) is formed at the entrance of the reaction channel. This complex was stabilized by hydrogen bonding (see NCI and AIM analyses, Fig. S2 and S3) and was located 3.75 kcal mol^{-1} below the reactant. The activation barrier height for TSA1 is approximately 6.08 kcal mol^{-1} above the reactant. After passing the barrier height, the product complex (PCA1) was found 11.88 kcal mol^{-1} below the reactants on the product side. It was stabilized by weak van der Waals interactions (see NCI analysis, Fig. S2). Eventually, the reaction results in the removal of water molecules and the formation of a radical product, cyc-$(CF_2)_4$CHO($^{\bullet}$)–. Its relative energy is lower than that of the reactant, 7.91 kcal mol^{-1}. Similarly, in the case of the A2 pathway, when hydrogen is abstracted from the methyne (C–H) position of cyc-$(CF_2)_4$CHOH– by OH radicals, the hydroxyl radicals form RCA2, which is stabilized by weak van der Waals (vdW) forces (see NCI and AIM analyses, Fig. S2 and S3). Their relative energies are approximately 1.47 kcal mol^{-1}; therefore, they are energetically more stable than the initial reactants. The A2 route (*via* TSA2) has a lower activation barrier of 1.62 kcal mol^{-1}, leading it to be more kinetically favorable than A1. The energy of its transition state is similar to that of the B2 route; however, B2 is significantly more advantageous because of its slightly lower barrier height. After passing the barrier, the system forms PCA2 and becomes more stable owing to hydrogen bonding (see NCI analysis, Fig. S2). PCA2 has a higher stability than the reactants by approximately 36.96 kcal mol^{-1}. The route produces the radical product cyc-$(CF_2)_4$C($^{\bullet}$)OH and a H_2O molecule, which are 27.55 kcal mol^{-1} below the reactants, indicating the high exergonicity of the channel. These results validate the thermodynamic and kinetic favorability of the A2 pathway.

Table 1 Reaction Gibbs free energy $(\Delta G^{\circ}_{298.15})$ and reaction enthalpy $(\Delta H^{\circ}_{298.15})$ for all pathways were calculated at the M06-2X/6-311+G(2d,2p) level, with MP2/6-311+G(2d,2p) values in parentheses, including scaled ZPE and SOC corrections (kcal mol^{-1})

Reaction system	$\Delta G^{\circ}_{298.15}$	$\Delta H^{\circ}_{298.15}$
Cyc-$(CF_2)_4$CHOH– + OH → cyc-$(CF_2)_4$CHO($^{\bullet}$)– + H_2O	−9.76 (−8.42)	−7.73 (−6.85)
Cyc-$(CF_2)_4$CHOH– + OH → cyc-$(CF_2)_4$C($^{\bullet}$)OH– + H_2O	−28.35 (−30.00)	−26.64 (−28.56)
Cyc-$(CF_2)_4$CHOH– + Cl → cyc-$(CF_2)_4$CHO($^{\bullet}$)– + HCl	1.20 (6.91)	4.04 (9.22)
Cyc-$(CF_2)_4$CHOH– + Cl → cyc-$(CF_2)_4$C($^{\bullet}$)OH– + HCl	−17.40 (−14.67)	−14.87 (−12.54)
Cyc-(CF_2)4CHOH– + OH → cyc-$CF_2CF_2CF_2CF(^{\bullet})$CHOH– + HOF	64.85 (65.71)	68.78 (68.86)
Cyc-$(CF_2)_4$CHOH– + Cl → cyc-$CF_2CF_2CF_2CF(^{\bullet})$CHOH– + ClF	50.86 (55.42)	55.56 (59.30)
Cyc-$(CF_2)_4$CHOH– + OH → cyc-$CF_2CF_2CF(^{\bullet})CF_2$CHOH– + HOF	64.23 (64.94)	67.68 (67.81)
Cyc-$(CF_2)_4$CHOH– + Cl → cyc-$CF_2CF_2CF(^{\bullet})CF_2$CHOH– + ClF	50.23 (54.65)	54.46 (58.26)

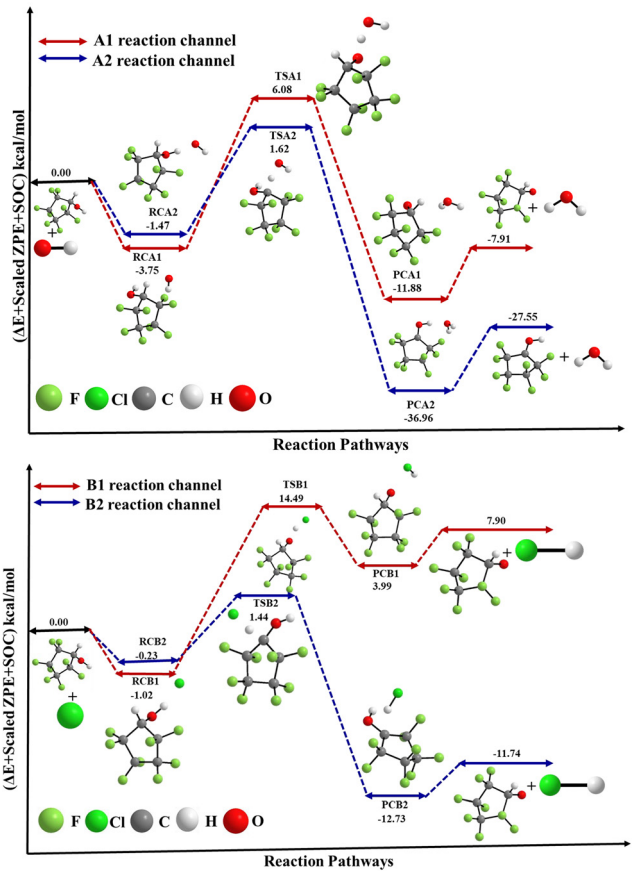

Fig. 1 Potential energy surface (PES) diagram of cyc-$(CF_2)_4CHOH$– degradation pathways at the CCSD(T)-MP2/CBS//M06-2X/6-311+G(2d,2p) level of theory.

3.2.2 Hydrogen abstraction *via* the Cl atom. In the B1 route, the Cl atom abstracts the hydroxyl hydrogen (O–H) of cyc-$(CF_2)_4CHOH$–, which starts with the formation of a weakly bound reactant complex (RCB1). When compared to the free reactants, this compound is weakly stabilized (1.02 kcal mol^{-1}). The highest activation barrier among the paths investigated is represented by the corresponding transition state (TSB1), which is located 14.49 kcal mol^{-1} above the reactants. Once the barrier is crossed, the system proceeds onto PCB1; however, this complex is not energetically stable, residing 3.99 kcal mol^{-1} above the reactants and is therefore prone to dissociation. Finally, the end products, cyc-$(CF_2)_4CHO(^{\bullet})$– and HCl, have a relative value of 7.90 kcal mol^{-1}, and they are themselves at higher energy than the reactants, making this route energetically unfavourable. In addition, the positive energy differences in the reaction Gibbs free energy $(\Delta G^{\circ}_{298.15})$ and enthalpy $(\Delta H^{\circ}_{298.15})$ demonstrate the endothermic and endergonic characteristics of the B1 channel, clearly establishing it as the least favorable reaction pathway from both kinetic and thermodynamic perspectives among all reaction pathways. In the B2 reaction route, the Cl atom abstracts a hydrogen atom from the C–H site of cyc-$(CF_2)_4CHOH$–, creating weakly stabilized RCB2 with a lower relative energy (0.23 kcal mol^{-1}). The subsequent transition state (TSB2) has a lower energy barrier of 1.44 kcal mol^{-1}, showing kinetically favorable behavior compared to the A1, A2 and B1 pathways. After surpassing the barrier, the system develops into a thermodynamically stabilized product complex (PCB2), which is 12.73 kcal mol^{-1} below the reactants. The channel yields radical species cyc-$(CF_2)_4C(^{\bullet})OH$– and HCl, with final products 11.74 kcal mol^{-1} lower in energy than the initial reactants, supporting the overall exergonic and kinetically accessible character of the process. To further demonstrate which reaction pathway was more favorable, we calculated the bond dissociation energies (BDEs) of the breaking C–H and O–H bonds at the M06-2X/6-311+G(2d,2p) level of theory. The BDEs of the O–H bond (117.10 kcal mol^{-1}) are approximately 19.32 kcal mol^{-1} greater than those of the C–H bond (97.78 kcal mol^{-1}), indicating that hydrogen abstraction from the C–H position dominates this reaction. This conclusion is supported by the rate coefficient data presented in the next section.

3.3 Kinetics

3.3.1 Methodology. The POLYRATE 2017-C program was used to study all H-abstraction reaction pathways.[54] Variational transition state theory (VTST) with an interpolated single-point energy (ISPE) technique was used to calculate the rate coefficients of all reaction pathways of the title processes. Rate coefficients are calculated using the canonical variational transition state theory (CVT) for the 220–420 K temperature range, considering atmospheric significance.[55–57] Two methods are used for tunneling corrections: zero-curvature tunneling (ZCT)[57–59] and small curvature tunneling (SCT).[60,61] CVT rate coefficients are derived by minimizing along dividing surface (s) at a given temperature (T). These are represented as follows:

$$k^{\mathrm{CVT}}(T) = \min k^{\mathrm{GT}}(T,s) \quad (2)$$

$$k^{\mathrm{GT}}(T,s) = \frac{\sigma k_{\mathrm{B}} T}{h}\frac{Q^{\mathrm{GT}}(T,s)}{\phi^{\mathrm{R}}(T)}\exp\left(-\frac{V^{\mathrm{CVT}}_{\mathrm{MEP}}(s)}{k_{\mathrm{B}}T}\right) \quad (3)$$

At the dividing surface, the rate coefficient of the generalized transition state theory is represented by the notation $k^{\mathrm{GT}}(T,s)$. The number of indistinguishable molecular orientations is represented by the quantity σ, which in this instance is assumed to be unity. Here, h and k_{B} stand for the Planck and Boltzmann constants, respectively. The partition function of the generalized transition state at surface s is described by the expression $Q^{\mathrm{GT}}(T,s)$, with reference to a local zero of energy specified at $V^{\mathrm{CVT}}_{\mathrm{MEP}}(s)$. $\phi^{\mathrm{R}}(T)$ is the partition function of reactants per unit volume. The $^2\Pi$ ground state of the OH radical exhibits spin–orbit splitting separated by approximately 140 cm^{-1} (0.20 kcal mol^{-1}), lowering the unperturbed $^2\Pi$ state to the $^2\Pi_{3/2}$ level.[45,62] Similarly, in the case of Cl atom, it exhibits two spin–orbit states, $^2p_{3/2}$ (degeneracy 4) and $^2p_{1/2}$ (degeneracy 2), separated by 882.4 cm^{-1} (0.8 kcal mol^{-1}).[45] In addition, the electronic partition function of the $^2\Pi_{3/2}$ and $^2\Pi_{1/2}$ states of OH and the $^2p_{3/2}$ and $^2p_{1/2}$ states of Cl, along with their respective energies and degeneracies, are included in the rate coefficient calculations.

The hydrogen abstraction reaction, R = cyc-$(CF_2)_4$CHOH– with Cl atoms and OH radicals, proceeded in the following stepwise sequence:

$$R + X \underset{k_{-1}}{\overset{k_1}{\rightleftharpoons}} RC \xrightarrow{k_2} \text{product}$$

where X = OH and Cl, k_1 and k_{-1} are the forward and reverse rate coefficients for the corresponding equilibrium between the reactant complex (RC) and the reactants cyc-$(CF_2)_4$CHOH–, OH, or Cl, and k_2 corresponds to the decomposition of the reactant complex to the final products *via* a barrier height (TS) for a particular reaction channel. Therefore, the overall rate coefficient $k^{GT}(T,s)$ was calculated using the steady-state approximation, as follows:

$$k^{GT}(T,s) = \frac{k_1}{k_{-1} + k_2} k_2 \quad (4)$$

Although the activation energy barrier for the dissociation of RC (k_{-1}) and its progression to products (k_2) are comparable, analysis reveals that the entropy change associated with the reverse reaction (k_{-1}) is considerably greater than the product formation (k_2). As a result, k_{-1} is likely to be significantly greater than k_2. This, coupled with the shallow well-depth (-0.23 to -3.72 kcal mol^{-1}) of the RC and collisional stabilization under tropospheric conditions, validates the implementation of the pre-equilibrium model (PEM)[63] within the Polyrate code.[64,65] With such a pre-equilibrium model (PEM), $k^{GT}(T,s)$ can be simplified to

$$k^{GT}(T,s) = \frac{k_1}{k_{-1}} k_2 = \left(\frac{A_1 A_2}{A_{-1}}\right) e^{\frac{-(E_1+E_2-E_{-1})}{RT}} = K_{eq} k_2 \quad (5)$$

Since E_1 is zero, the net activation energy for the overall reaction is

$$E_a = (E_2 - E_{-1}) = (E_{TS} - E_{RC}) - (E_{RC} - E_R) = (E_{TS} - E_R) \quad (6)$$

Utilizing basic statistical thermodynamic principles, here K_{eq} is the equilibrium constant for the formation of RC from reactants. K_{eq} and k_2 are defined as follows:[66]

$$K_{eq} = \frac{Q^{RC}}{\phi^R(T)} \exp\left(-\frac{E^{RC} - E^R - E^X}{k_B T}\right) \quad (7)$$

$$k_2 = \kappa_T \frac{\sigma k_B T}{h} \frac{Q^{GT}(T,s)}{Q^{RC}} \exp\left(-\frac{E^{TS} - E^{RC}}{k_B T}\right) \quad (8)$$

Notably, when eqn (7) and (8) are substituted into eqn (5), the results are identical to eqn (3), $k^{GT}(T,s)$. Therefore, to calculate the rate coefficient, the reaction is effectively treated as an elementary step R → TS → P, and $k^{GT}(T,s)$ from eqn (3) is used directly.[67] The κ_T is the only exception, as its value is determined by the activation barrier of the elementary process within which the hydrogen atom is abstracted.[67] Subsequently, to account for tunneling, the CVTST rate coefficients were adjusted using κ_T, calculated *via* the ZCT and SCT techniques. The CVT/SCT rate coefficients were fitted within the 220–420 K range using the modified Arrhenius expression.

$$k = A T^n \exp\left(\frac{-E_a}{RT}\right) \quad (9)$$

In eqn (9), T corresponds to temperature, n is the temperature exponent, R is the universal gas constant, E_a is the activation barrier, and A is the Arrhenius prefactor.

3.3.2 Rate coefficient calculation. Considering the two reaction channels for each reaction of cyc-$(CF_2)_4$CHOH– with Cl atoms and OH radicals, the total rate coefficient was obtained as follows:

$$k_{AT} = k_{A1} + k_{A2} \quad (10)$$

$$k_{BT} = k_{B1} + k_{B2} \quad (11)$$

The rate coefficient for hydrogen abstraction from the hydroxyl hydrogen (O–H) position is k_{A1} and k_{B1}, whereas the rate coefficient for hydrogen abstraction from the methine (C–H) site of the cyc-$(CF_2)_4$CHOH– molecule is k_{A2} and k_{B2}. The overall rate coefficients for the OH radicals and Cl atoms are represented by k_{AT} and k_{BT}, respectively.

As discussed in the preceding section, the substantial bond dissociation energy (BDE) of the hydroxyl O–H site of cyc-$(CF_2)_4$CHOH–, together with the similarly high activation barrier, renders this abstraction pathway kinetically less favorable than the C–H site. Therefore, hydrogen abstraction from the C–H site (pathways A2 and B2) is considered to have a significant impact on the rate coefficients and lifetime values of cyc-$(CF_2)_4$CHOH–. Here, the ISPE technique was used to determine temperature-dependent rate coefficients. The frequencies and geometries of the stationary points for the ISPE technique were estimated using the M06-2X/6-311+G(2d,2p) method. The reaction energies and barrier heights were improved utilizing the CBS extrapolation method, and the rate coefficients were estimated in the 220–420 K range using variational transition state theory (VTST). The CVT/SCT rate coefficients for the reaction of cyc-$(CF_2)_4$CHOH with OH radicals and Cl atoms over 220–420 K are depicted in Fig. 2(a) and (b). In Fig. S5, the rate coefficients for CVT, CVT/SCT, and CVT/ZCT are plotted for each reaction pathway.

The CVT/SCT rate coefficients for the overall reaction and each reaction channel of the cyc-$(CF_2)_4$CHOH– + OH reaction are shown in Fig. 2(a). Fig. 2(a) and Fig. S6 show that reaction pathway A1 exhibits a positive temperature dependency, which is a feature of a classical over-the-barrier reaction, in which thermal activation causes the rate coefficient to increase with increasing temperature. However, reaction route A2's lower barrier height enhances the quantum tunneling contributions, especially at low temperatures 220 to 275 K. Consequently, there seems to be a negative temperature dependency in the rate coefficients derived from the CVT/SCT and CVT/ZCT computations, which shows an inverse temperature dependence in comparison with the CVT findings. This behavior can be attributed to the fact that, within this temperature range, the tunneling contribution diminishes more rapidly with increasing temperature than in the traditional over-the-barrier

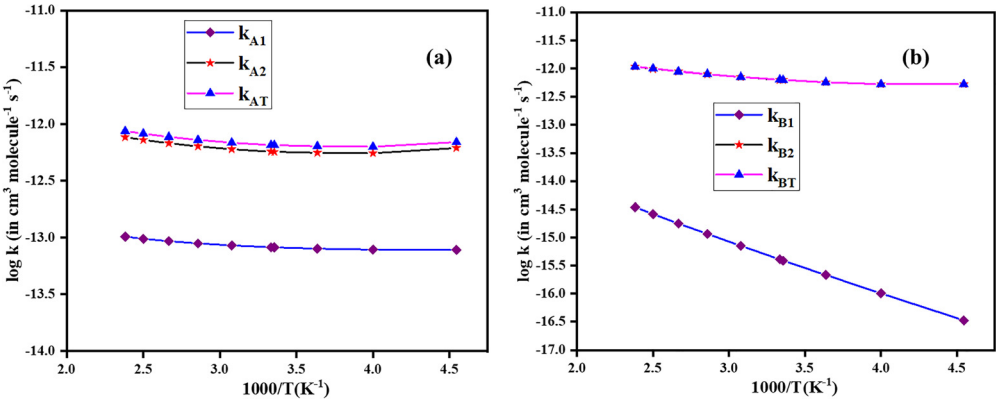

Fig. 2 CVT/SCT rate coefficients for the (a) cyc-$(CF_2)_4$CHOH– + OH and (b) cyc-$(CF_2)_4$CHOH– + Cl reactions, plotted as a function of 1000/T over 220–420 K, calculated at the CCSD(T)-MP2/CBS//M06-2X/6-311+G(2d,2p) level.

process. Over the range of 275–420 K, the reaction kinetics gradually shifted toward a positive, Arrhenius-type temperature dependency, with thermal activation taking over as the predominant process. Because the A1 reaction route has a significantly higher activation energy barrier than the A2 pathway, it is kinetically less preferred and has a lower calculated rate coefficient value. The degradation pathways were the H-abstraction reactions of cyc-$(CF_2)_4$CHOH– with the OH radicals, as demonstrated by the rate coefficient data tabulated in Table S4. At 296 K, the reaction rate coefficient of cyc-$(CF_2)_4$CHOH– with the OH radical is 6.5×10^{-14} cm^3 molecule^{-1} s^{-1} based on the quasi-theoretical methodology studied by Imasu *et al.*[23] The A1 route, which includes hydrogen abstraction at the O–H site of cyc-$(CF_2)_4$CHOH–, has a rate coefficient of 8.21×10^{-14} cm^3 molecule^{-1} s^{-1} at CBS levels, calculated at 298 K, which is roughly on the same order of magnitude as that in earlier research.[23] The total rate coefficient measured at 298 K was 5.68×10^{-13} cm^3 molecule^{-1} s^{-1}, which is approximately ten times higher than the previously published data.[23]

Fig. 2(b) shows the CVT/SCT rate coefficients of the cyc-$(CF_2)_4$CHOH– + Cl reaction, for both the overall reaction and each reaction channel. The results are presented in Table S5. Fig. 2(b) and Fig. S6 show the rate coefficients of the reaction channels B1 and B2 (CVT, CVT/SCT, and CVT/ZCT), and the overall results show a positive temperature dependence. Compared with B2, the B1 reaction pathway has a substantially greater energy barrier, causing it to proceed more slowly. In contrast, the B2 route has a lower transition-state energy, which makes it more kinetically favorable and increases the reaction rate. The rate coefficient for H-abstraction from the C–H site by the OH radical is 6.92 times larger than that from the O–H site, according to computational calculations that quantify this selectivity at 298 K. Furthermore, the Cl atom exhibited comparable reactivity to the OH radical towards the C–H site, with a slightly higher rate coefficient (k_{B2}/k_{A2} = 1.11). Utilizing the CVT/SCT technique, the revised Arrhenius parameters for the cyc-$(CF_2)_4$CHOH– reactivity toward both OH radicals and Cl atoms are tabulated in Table S7. These parameters provided a more accurate description of the temperature-dependent kinetics of each reaction pathway. The three-parameter equations were derived for the temperature range of 220–420 K in order to quantitatively characterize the temperature dependency of the rate coefficients (cm^3 molecule^{-1} s^{-1}):

$$k_{AT} = 4.41 \times 10^{-23} \times T^{3.55} \times e^{\frac{949.12}{T}} \quad (12)$$

$$k_{BT} = 6.83 \times 10^{-24} \times T^{3.94} \times e^{\frac{835.42}{T}} \quad (13)$$

The temperature dependence of the rate coefficients can be adequately explained using these equations.

3.4 Branching ratio

The ratio of the rate coefficient for each reaction channel to the total rate coefficient is known as the branching ratio. Fig. 3 shows a plot of the branching ratios of cyc-$(CF_2)_4$CHOH– to the OH radicals and Cl atoms. In both reactions, hydrogen abstraction from the C–H group (A2 and B2) was found to be the most important pathway. As shown in Fig. 3(a) and (b), hydrogen abstraction from the C–H group (A2) was the dominant route, with a branching ratio greater than that of A1 (hydrogen abstraction from the O–H group). Similarly, in the case of cyc-$(CF_2)_4$CHOH– with a Cl atom, the branching ratio of B2 (hydrogen abstracted *via* the C–H position) is more contributing than B1 (hydrogen abstracted *via* the O–H position).[68] The branching ratio for hydrogen abstraction pathways involved in reactions A1 and A2 at 298 K was calculated to be 12.6% and 87.4% respectively. Pathway A1 provides around 11–13% over the temperature range of 220 to 420 K, according to the branching ratio analysis, whereas pathway A2 dominates with an 88–89% contribution. The H-atom abstraction reaction for pathway B1 contributed minimally to the overall rate coefficients in the examined range, whereas pathway B2 was a significant contributor to both B1 and B2 (cyc-$(CF_2)_4$CHOH– + Cl). For pathway B2, the branching ratio is estimated to be approximately 100% at all temperatures. A carbon-centered radical is created when an H atom is extracted from the C–H position by an OH radical or Cl atom, whereas an oxygen-centered radical is created when it is abstracted from the O–H position. The radicals created from the carbon-centered radical were more stable than those formed from the oxygen-centered radical because the carbon-centered radicals were more

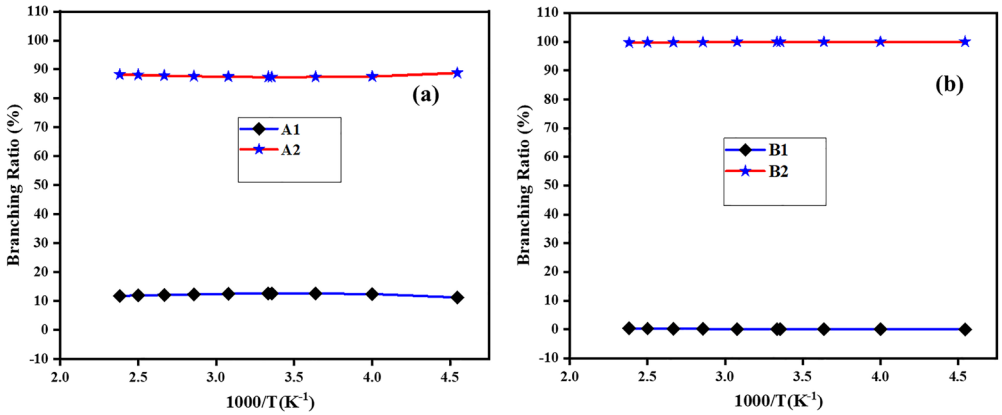

Fig. 3 Branching ratios based on CVT/SCT rate coefficients for (a) OH + cyc-$(CF_2)_4$CHOH– and (b) Cl + cyc-$(CF_2)_4$CHOH– reactions, shown as a function of 1000/T over 220–420 K.

polarizable.[14] Table 2 provides a summary of the overall rate coefficients of the title reactions and reactions of different comparable cyclic alcohols with OH radicals at 298 K. When we compared the experimentally determined rate coefficient of cyc-(C_4H_8)CHOH– with the calculated value of cyc-(C_4F_8)CHOH–, we found that fluorination reduced the rate constant. However, our calculated data did not fit the theoretically derived data for cyc-(C_4H_8)CHOH–.

4. Atmospheric implications

4.1 Atmospheric lifetime

It was expected that the rate coefficients for the reactions between cyc-$(CF_2)_4$CHOH–, NO_3 and O_3 would be lower than those with OH radicals and Cl atoms. Thus, cyc-$(CF_2)_4$CHOH– degradation due to interactions with O_3 molecules and NO_3 radicals contributed negligibly to the overall atmospheric lifetime. The following equation was used to determine the lifetime of cyc-$(CF_2)_4$CHOH– with respect to the reaction between the Cl atoms and OH radicals:

$$\tau_{OH} = (k_{OH} \times [OH])^{-1} \quad (14)$$

$$\tau_{Cl} = (k_{Cl} \times [Cl])^{-1} \quad (15)$$

Hence, the atmospheric lifetime of cyc-$(CF_2)_4$CHOH– was estimated using OH (τ_{OH}) and Cl (τ_{Cl}). Two types of chlorine concentration were considered: one at the marine boundary layers (1.0×10^5 molecules per cm^3)[73] and the other at the global average concentration (1.0×10^3 molecules per cm^3).[74] The atmospheric concentration of OH radicals is approximately 1×10^6 molecules per cm^3.[75] The overall rate coefficient for the reaction of cyc-$(CF_2)_4$CHOH– with OH radicals, determined at the CBS level, is $k_{AT} = 6.50 \times 10^{-13}$ cm^3 $molecule^{-1}$ s^{-1}. By utilizing all these values, the calculated lifetime of cyc-$(CF_2)_4$CHOH– was approximately 17.8 days at a global average concentration of OH radicals. Similarly, the calculated overall rate coefficient with Cl atoms was $k_{BT} = 6.33 \times 10^{-13}$ cm^3 $molecule^{-1}$ s^{-1}. This yields a considerably longer lifetime of the cyc-$(CF_2)_4$CHOH– compound, approximately 50.1 years with Cl atoms at the global average concentration, and 0.50 years with Cl atoms at marine boundary layers, respectively.

To investigate the impact of atmospheric variables, including temperature, altitude, and radical concentration, the specific lifetimes of cyc-$(CF_2)_4$CHOH– are shown in Fig. 4 and Tables S8, S9. According to the rate coefficient calculated at the CCSD(T)-MP2/CBS//M06-2X/6-311+G(2d,2p) level of theory, the τ values predicted by various OH concentrations in the troposphere (9.00×10^5 to 1.50×10^7 molecule cm^{-3})[76,77] at different altitudes in the Earth's atmosphere (from 0 to 10 km) correspond to temperatures ranging from 298.15 to 223.29 K, respectively. Fig. 4 and Table S7 show that the OH-controlled atmospheric lifetimes of cyc-$(CF_2)_4$CHOH– vary from 1.14 days to 20.48 days within 223.29–298.15 K when the altitude is 0–10 km and the OH radical concentration is 9.00×10^5 to 1.50×10^7

Table 2 Comparison of OH radical reaction rate coefficients at 298 K for selected cyclic alcohols, including the cyc-(C_4F_8)CHOH– compound

Species	Techniques	cm^3 $molcule^{-1}$ s^{-1}	Ref.
Cyc-(C_5H_{10})CHOH–	Relative rate	$(1.90 \pm 4.8) \times 10^{-11}$	Bradley *et al.*[69]
Cyc-(C_4H_8)CHOH–	Resonance fluorescence	$(1.07 \pm 0.7) \times 10^{-11}$	Wallington *et al.*[70]
	Theory	3.35×10^{-15}	Hatipoğlu *et al.*[71]
Cyc-(C_3H_6)CHOH–	Theory	1.88×10^{-16}	Hatipoğlu *et al.*[71]
Cyc-(C_2H_4)CHOH–	Theory	1.52×10^{-17}	Hatipoğlu *et al.*[71]
Cyc-(C_4F_8)CHOH–	Quasi-theoretically[a]	6.50×10^{-14}	Imasu *et al.*[23]
Cyc-(C_4F_8)CHOH–	Theory	5.68×10^{-13}	This work
(*E*)-4-Methylcyclohexanol	Relative rate	$(1.87 \pm 0.14) \times 10^{-11}$	Colmenar *et al.*[72]

[a] This value was calculated at 296 K.

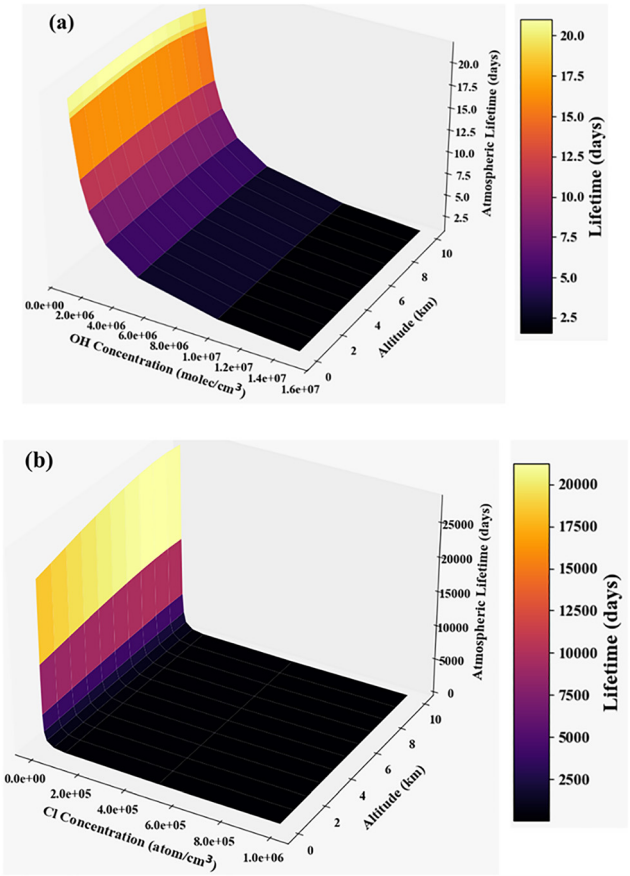

Fig. 4 The atmospheric lifetimes (τ) of cyc-$(CF_2)_4$CHOH– were determined at different altitudes (H), based on the computed CVT/SCT rate coefficients: (a) with OH radicals and (b) with Cl atoms.

molecule cm^{-3}.[76,77] The Cl-controlled atmospheric lifetime of cyc-$(CF_2)_4$CHOH– is 18.24 to 2.21 × 10^4 days (tabulated in Table S8) within the altitude range of 0–10 km and the Cl atom concentration is 1.00 × 10^3 to 1.00 × 10^6 atom cm^{-3}. At fixed altitudes, increasing concentrations of OH radicals or Cl atoms contribute to a gradual decrease in the atmospheric lifetime (see Tables S8 and S9) of cyc-$(CF_2)_4$CHOH–, underscoring the dominant influence of both oxidants on its atmospheric fate.

To look into this more, the contribution of OH radical and Cl atom, the OH-controlled lifetime, Cl-controlled lifetime, and τ_{eff} of cyc-$(CF_2)_4$CHOH– at a minimum OH concentration of 9.00 × 10^5 molecule cm^{-3} and a maximum Cl concentration of 1.00 × 10^6 atom cm^{-3} were computed as shown in Fig. 5. The effective lifetime (τ_{eff}) of cyc-$(CF_2)_4$CHOH– in the atmosphere was evaluated using the following formula:

$$\tau_{eff} = \left[\frac{1}{\tau_{OH}} + \frac{1}{\tau_{Cl}}\right]^{-1} \quad (16)$$

Fig. 5 shows that the atmospheric lifetime (τ_{OH} and τ_{Cl}) of cyc-$(CF_2)_4$CHOH– varies slightly with the altitude in the troposphere. The τ_{OH} remains relatively constant for approximately 20 days up to ~4 km and gradually declines at higher altitudes,

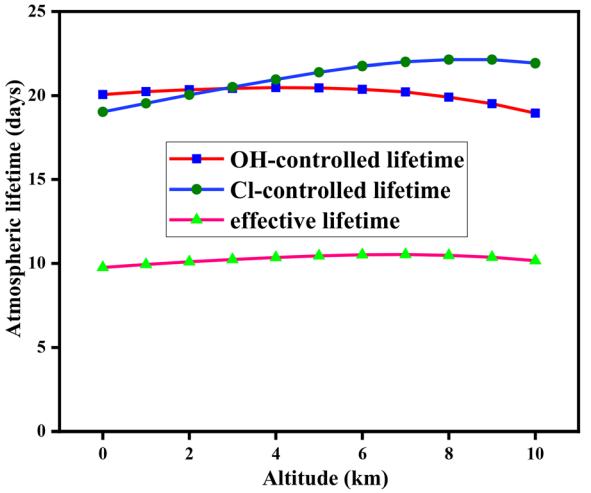

Fig. 5 The cyc-$(CF_2)_4$CHOH– compound's OH-controlled lifetime, Cl-controlled lifetime, and τ_{eff} were calculated using an OH radical concentration of 9.00 × 10^5 molecule cm^{-3} and a Cl concentration of 1.00 × 10^6 atom cm^{-3}. At the CCSD(T)-MP2/CBS//M06-2X/6-311+G(2d,2p) level, the rate coefficients were computed.

showing accelerated oxidative loss in areas with elevated OH reactivity. In contrast, τ_{Cl} increases gradually with altitude, showing that chlorine-initiated oxidation has a lower impact at higher elevations. Across all altitudes, the effective lifetime (τ_{eff}), based on both the OH and Cl processes, seems identical at approximately 10 days. The effective lifetime (τ_{eff}) value indicates that cyc-$(CF_2)_4$CHOH– has reduced atmospheric persistence. While both oxidants contribute to its elimination, OH-initiated oxidation predominates under normal tropospheric circumstances due to its higher concentration in the atmosphere.

4.2 Atmospheric implication parameters

Furthermore, to determine the effect of this compound on the troposphere, we calculated different atmospheric implication parameters such as radiative efficiency (REs), global warming temperature (GWP), global temperature change potential (GTP), integrated global temperature change potential (iGTP), photo ozone creation potential (POCP), and acidification potential (AP), which are discussed in detail in the SI. We performed our frequency calculation to determine the absorption cross-section and radiative efficiency at the B3LYP/6-31G(d,p) level of theory, which is the most trustworthy approach for atmospheric implication calculations.[31,32,78–80] We computed an absorption cross-section area of 26.9 × 10^{-17} cm^2 $molecule^{-1}$ cm^{-1} of cyc-$(CF_2)_4$CHOH– in the wavenumber range of 0–2500 cm^{-1}, approximately closer to previously published data (21.1 × 10^{-17} cm^2 $molecule^{-1}$ cm^{-1}).[24] Using the absorption cross-section, which is given in Fig. 6, we calculated the instantaneous and lifetime corrected RE values (a detailed analysis is provided in the SI). Lifetime-corrected REs are quite small (0.062 W m^{-2} ppb^{-1}), and instantaneous REs are 0.36 W m^{-2} ppb^{-1}. The contribution of cyc-$(CF_2)_4$CHOH– to global warming potential (GWP) may not be significant because of the short atmospheric effective lifetime

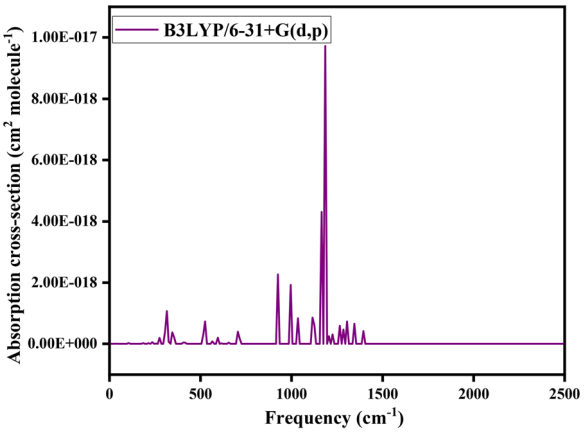

Fig. 6 Infrared absorption cross-section spectra of cyc-$(CF_2)_4$CHOH– at the B3LYP/6-31G(d,p) level.

(τ_x) of an OH-controlled process and a Cl-controlled process. Additional computed values, such as GTP and iGTP, are tabulated in Table S10. We also determined the photo-ozone formation potential (POCP) for cyc-$(CF_2)_4$CHOH–, which is approx. 12.7, whereas the POCP of ethane is 12.3. Since ethane and methane oxidize so slowly, they are typically not a major source of local air quality issues and are therefore not subject to air quality legislation.[81] The POCP values for cyc-$(CF_2)_4$CHOH– are negligible in comparison with the reference chemical ethene (C_2H_4), which has a POCP value of 100. Therefore, we conclude that commercially important cyc-$(CF_2)_4$CHOH– does not play a major role in tropospheric ozone generation. As a result, cyc-$(CF_2)_4$CHOH– does not present any serious risks to the tropospheric vegetation growth, animal health, or the human population. Additionally, the analysis of potential acidification values showed that cyc-$(CF_2)_4$CHOH– has a larger acidifying capability than SO_2 (AP = 1), with an acidification potential (AP) value of 1.40. According to the value, acid rain incidents that are seen in polluted regions may be disrupted if these compounds are removed from the air by wet deposition processes.[82–84]

5. Dielectric strength (DS)

We used the DFT-based theoretical method B3LYP/6-311+G(d,p) to determine the dielectric strength (DS) of cyc-$(CF_2)_4$CHOH–. According to a previously published study, the B3LYP/6-311+G(d,p) level of theory is the most efficient DFT method for determining the dielectric strength (DS).[85–88] Several parameters, such as molecular mass, polarizability, ionization energy, and electron affinity, influence the dielectric constant of organic compounds. Polarizability and ionization energy are the primary variables that affect the dielectric strength. Notwithstanding the contributions of each of the previously mentioned components.[89] The expression for the DS equation is as follows:

$$DS = 0.0012 \times \alpha^{1.181} \times \varepsilon^{1.768} \quad (17)$$

In this context, DS represents the dielectric strength, and the term ''ionization energy'' (ε) describes the change in Gibbs free energy that occurs when an electron is extracted from a molecule. The polarizability of an organic compound is represented by α. In addition, the parameterized coefficients in the equation for the precise prediction of organic molecules introduced in published literature are 0.0012, 1.181, and 1.768.[89] A new variable molecular weight (M_w) is added in the previous equation to get more accurate dielectric strength (DS), and the resulting equation is as follows:[88]

$$DS = 0.0012 \times \alpha \times \varepsilon^{0.288} \times M_w^{0.401} \quad (18)$$

We obtained the DS values of cyc-$(CF_2)_4$CHOH– using eqn (17) and (18). Using eqn (17), we obtained 1.174, and using eqn (18), we obtained 0.201. Because both have lower dielectric strengths than SF_6, neither can replace the SF_6 molecule (DS = 0.7121) according to our estimated data.

6. Atmospheric fate

The most favorable pathway for both Cl atoms and OH radicals is hydrogen abstraction from the C–H position, according to our calculated thermodynamic quantities, such as reaction Gibbs free energy ($\Delta G^{\circ}_{298.15}$), reaction enthalpy ($\Delta H^{\circ}_{298.15}$), bond dissociation energies (BDEs), and reaction kinetics. Furthermore, hydrogen abstraction with OH radicals and Cl atoms results in the formation of cyc-$(CF_2)_4$C(•)OH– radicals, H_2O, and HCl compounds. After the formation of alkyl radical cyc-$(CF_2)_4$C(•)OH–, we examined the alkyl radical degradation process in more detail. The reaction enthalpy ($\Delta H^{\circ}_{298.15}$) and Gibbs free energy ($\Delta G^{\circ}_{298.15}$), including scaled ZPE of the radical product, are −39.13 kcal mol^{-1} and −41.35 kcal mol^{-1}, respectively, indicating that the process is exothermic and spontaneous, favourable for further investigation of its degradation. As demonstrated by da Silva *et al.*[90] and Zádor *et al.*,[91] an alcohol-specific reaction channel is considered for the 1-hydroxycyclopentyl radical. The addition of O_2 to the cyc-$(CF_2)_4$C(•)OH– radical proceeds *via* a barrierless route, forming a stabilized peroxy intermediate (IM1). The computed relative energies of IM1 are lower in comparison with reactants and are 58.91 kcal mol^{-1} at the CBS levels. Then the reaction goes through a transition state (TSa), with activation barriers of 34.50 kcal mol^{-1} relative to IM1, indicating a moderately hindered process. Finally, the reaction exit through the resulting product complex, PCa, lies lower in energy than the reactants by 49.01 kcal mol^{-1}, confirming the thermodynamic favorability of the pathway. The system eventually transforms into a stable product, perfluorinated cyclopentanone, and HO_2 radical, with relative energies of 45.03 kcal mol^{-1} as compared to the reactants, indicating that the degradation pathway is generally exothermic (Fig. 7).

7. MD simulation of nucleation

A gas-phase system consisting of one cyc-$(CF_2)_4$CHOH– molecule, 9 H_2SO_4 (SA) molecules, 154 N_2 molecules, and 41 O_2 molecules was used for molecular dynamics (MD) simulations

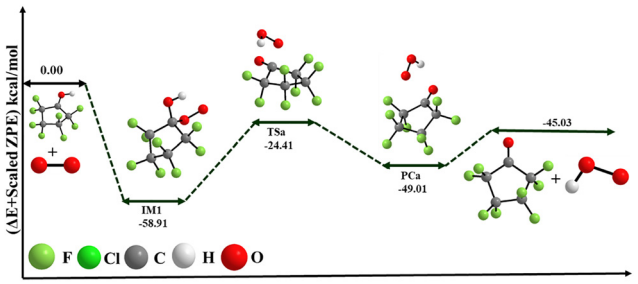

Fig. 7 PES diagram of radical product degradation pathways at the CCSD(T)-MP2/CBS//M06-2X/6-311+G(2d,2p) level of theory.

in order to examine the nucleation potential of the chemical. The generation of secondary organic aerosols (SOAs) frequently involves particle nucleation, including SA, NH_4^+, and NO_3^-. When it comes to neutral nucleation, SA is recognized to be more efficient than the ion-induced model.[92] Thus, the interactions between SA and cyc-$(CF_2)_4$CHOH– were the main focus of this study. In Fig. 8, the snapshots of the SA-cyc-$(CF_2)_4$CHOH–N_2–O_2 system at different times are shown. At t = 0 ns, the system displayed scattered molecules without clustering. By t = 2.5 ns, the primary molecule was still not involved, but early SA-only clusters, such as $(SA)_3$ and $(SA)_2$, had appeared. A larger cluster with up to eight SA molecules was observed between 5 and 10 ns. The first significant compound, cyc-$(CF_2)_4$CHOH, which included all 9 SA molecules, formed at t = 15 ns. Incredibly, only a (SA)9 cluster remained at t = 20 ns, whereas the main molecule was abruptly excluded. However, a stable cluster consisting of 9 SA molecules and cyc-$(CF_2)_4$CHOH– was developed and remained between 30 and 40 ns. Strong electrostatic and hydrogen bonding interactions between the cyc-$(CF_2)_4$CHOH and SA molecules can result in the formation of larger and more stable clusters. The nucleating cluster stability was quantified by calculating the radial distribution function, $g(r)$, between the cyc-$(CF_2)_4$CHOH and the surrounding sulfuric acid (SA) molecules throughout the equilibrated trajectory time (37–40 ns). The resultant $g(r)$ plot (see Fig. S7) shows a strong, intense peak at 0.3–0.8 nm with a magnitude greater than 2200, indicating that SA is most likely to occur around the cyc-$(CF_2)_4$CHOH compound.[93] It should be mentioned that the NPT simulation duration was limited to 40 ns, following the standard procedures used in corresponding studies.[92,94,95] This time frame was adequate to accomplish convergence and capture the system's equilibrium state. However, to investigate the slower nucleation dynamics and confirm the validity of these results, future research could prolong the simulation time. According to these findings, cyc-$(CF_2)_4$CHOH– may be relevant in the production of atmospheric new particles as it may take part in SA-mediated nucleation under neutral circumstances.

8. Toxicity assessment

The ECOSAR program[64] was used to assess the acute and chronic toxicity of cyc-$(CF_2)_4$CHOH– and its degradation products. Three nutrient levels, fish, *Daphnia*, and green algae, were used to evaluate their effects on aquatic and chronic toxicity. For fish and *Daphnia*, acute toxicity was measured using the median lethal concentration (LC_{50}) after 96 and 48 h of exposure, respectively. For green algae, half the maximum effective concentration (EC_{50}) was reached after 96 h of exposure. Additionally, the chronic toxicities of the three aquatic organisms were represented by their chronic toxicity values (ChV). It is considered harmful when $1 < ChV < 10$ mg L^{-1} (chronic toxicity) and $10 < LC_{50}$ or $(EC_{50}) < 100$ mg L^{-1} (acute toxicity).

Therefore, the computed acute and chronic toxicities of cyc-$(CF_2)_4$CHOH– of median fatal concentration value are 196 mg L^{-1} and 111 mg L^{-1}, and its chronic toxicity value is 19.1 and 10.8 mg L^{-1} for fish and *Daphnia*, which is higher than the range of toxicity standards, indicating that this molecule has no detrimental effects on fish. However, in the case of green algae, the maximum effective concentration (EC_{50}) is lower than

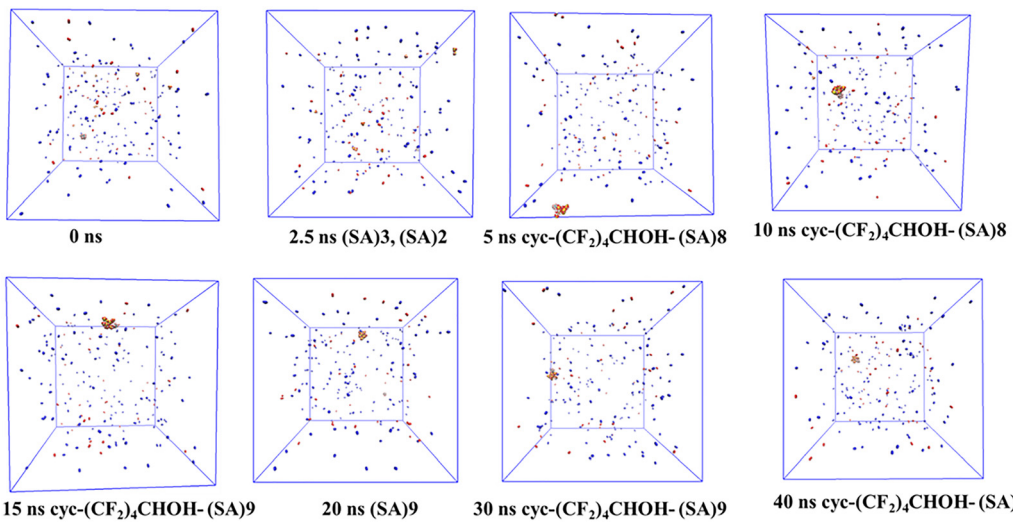

Fig. 8 A collection of snapshots from the NPT simulation system. SA, N_2, O_2, and cyc-$(CF_2)_4$CHOH– were depicted using the VMD rendering technique.

(EC_{50}) < 100 mg L^{-1}, 82.1 mg L^{-1} value is harmful, and in the case of chronic toxicity (ChV < 10 mg L^{-1}), the value is higher, around 21.4 mg L^{-1}, which means that there is no harmful effect on algae. The degradation product fluorinated cyclopentanone values for both acute and chronic toxicity were higher in this range when 1 < ChV < 10 mg L^{-1} (chronic toxicity) and 10 < LC_{50} or (EC_{50}) < 100 mg L^{-1}. Thus, fluorinated cyclopentanones have no effect on aquatic organisms. These findings suggest that, compared to the parent chemicals, cyc-$(CF_2)_4$CHOH–, the transformation products, cyc-$(CF_2)_4$C(O)–, are less harmful to aquatic organisms.

9. Conclusions

Mechanistic and kinetic studies of cyc-$(CF_2)_4$CHOH– with OH radicals and Cl atoms were conducted with the support of DFT and canonical variational transition state theory. High-level DFT techniques and CBS extrapolation were used to assess the rate coefficients and thermochemical parameters of the reaction of cyc-$(CF_2)_4$CHOH– with OH radicals and Cl atoms to ensure reliable and precise predictions. Two hydrogen abstractions are possible from cyc-$(CF_2)_4$CHOH–: one from the O–H position and the other from the C–H position. All reaction pathways that result in the reaction of cyc-$(CF_2)_4$CHOH– with OH radicals are exothermic $\left(\Delta H^{\circ}_{298.15} < 0\right)$ and exergonic $\left(\Delta G^{\circ}_{298.15} < 0\right)$. However, it was found that a Cl atom's hydrogen abstraction from the hydroxyl group of cyc-$(CF_2)_4$CHOH– was endothermic and endergonic in nature, illustrating that the B1 pathway is both thermodynamically and kinetically unfavorable. The canonical variational transition state theory (CVT) with small-curvature tunneling (SCT) using the M06-2X technique was used to obtain the theoretical rate coefficient for each reaction channel at temperatures of 220–420 K. In accordance with the branching ratios, the A2 and B2 reaction routes were dominant for the reactions of cyc-$(CF_2)_4$CHOH– with OH radicals and Cl atoms, indicating that their rate coefficient values were higher than those of the other pathways. At temperatures of 223.29 and 298.15 K and 0–10 km altitude, the predicted OH-driven and Cl-driven lifetime variations of cyc-$(CF_2)_4$CHOH– vary from 1.14 days to 20.48 days and from 18.24 to 2.21 × 10^4 days, respectively. Owing to the lower effective lifetime (τ_x) of cyc-$(CF_2)_4$CHOH–, its GWP, GTP, and iGTP are insignificant, indicating a small influence on climate change. Although our calculated POCP value is not sufficient when compared to alkenes (POCP = 100), there is no adverse effect on the formation of smog in the atmosphere. However, the acidification potential (AP) we determined is notable when compared to that of SO_2, which raises environmental concerns. Owing to their lower DS values, our compounds could not replace SF_6 in the dielectric strength evaluation. Furthermore, classical MD simulations have shown that the primary component, cyc-$(CF_2)_4$CHOH–, is associated with H_2SO_4 and participates in the early stages of NPF growth. Based on these facts, this study can help us better comprehend cyc-$(CF_2)_4$CHOH– and provide a representative model for studying additional halogenated cycloalcohols.

Author contributions

Suresh Tiwari: conceptualization, methodology, writing – original draft preparation, formal analysis, reviewing, and editing. Ranga Subramanian: conceptualization, methodology, formal analysis, supervision, reviewing, and editing.

Conflicts of interest

The authors declare that they have no conflicts of interest.

Data availability

The data supporting this article have been included as part of the supplementary information (SI). Supplementary information is available. See DOI: https://doi.org/10.1039/d5cp02637g.

Acknowledgements

As part of the special edition of Physical Chemistry Chemical Physics, the authors address this work to Professor Narayanasami Sathyamurthy on the celebration of his 75th birthday. His groundbreaking work in theoretical and computational chemistry continues to motivate future generations of researchers in this field. As well, S. T. thanks the Indian Institute of Technology Patna for providing Supercomputer Paramrudra facilities and financial support to carry out this work.

References

1 A. McCulloch, P. M. Midgley and P. Ashford, *Atmos. Environ.*, 2003, **37**, 889–902.
2 A. McCulloch, *J. Fluorine Chem.*, 1999, **100**, 163–173.
3 T. J. Wallington, W. F. Schneider, D. R. Worsnop, O. J. Nielsen, J. Sehested, W. J. Debruyn and J. A. Shorter, *Environ. Sci. Technol.*, 1994, **28**, 320A–326A.
4 M. Grubb, C. Vrolijk and D. Brack, *Routledge revivals: Kyoto Protocol (1999): A guide and assessment*, Routledge, 2018.
5 S. Solomon and J. S. Daniel, *Clim. Change*, 1996, **32**, 7–17.
6 G. Ghani, *Econ. Bull.*, 2007, **17**, 1–5.
7 B. Baidya, M. Lily and A. K. Chandra, *ChemistrySelect*, 2019, **4**, 7134–7143.
8 A. Sekiya and S. Misaki, *J. Fluorine Chem.*, 2000, **101**, 215–221.
9 K. Kambanis, Y. Lazarou and P. Papagiannakopoulos, European Commission: Belgium, 1998, p. 557.
10 E. Jiménez, M. Antiñolo, B. Ballesteros, E. Martínez and J. Albaladejo, *ChemPhysChem*, 2010, **11**, 4079–4087.
11 P. J. Godin, K. Le Bris and K. Strong, *J. Quant. Spectrosc. Radiat. Transfer*, 2017, **203**, 522–529.
12 S. Gligorovski, R. Strekowski, S. Barbati and D. Vione, *Chem. Rev.*, 2015, **115**, 13051–13092.
13 H. Singh and J. Kasting, *J. Atmos. Chem.*, 1988, **7**, 261–285.
14 A. Kumar, S. Gonu, S. Vijayakumar, C. Ramya and B. Rajakumar, *J. Phys. Chem. A*, 2021, **125**, 523–535.

15 K. T. Malecha and S. A. Nizkorodov, *J. Phys. Chem. A*, 2017, **121**, 4961–4967.
16 M. Kulmala, H. Vehkamäki, T. Petäjä, M. Dal Maso, A. Lauri, V.-M. Kerminen, W. Birmili and P. McMurry, *J. Aerosol Sci.*, 2004, **35**, 143–176.
17 M. Kulmala, J. Kontkanen, H. Junninen, K. Lehtipalo, H. E. Manninen, T. Nieminen, T. Petäjä, M. Sipilä, S. Schobesberger and P. Rantala, *Science*, 2013, **339**, 943–946.
18 R. Zhang, A. Khalizov, L. Wang, M. Hu and W. Xu, *Chem. Rev.*, 2012, **112**, 1957–2011.
19 M. Sipilä, T. Berndt, T. Petäjä, D. Brus, J. Vanhanen, F. Stratmann, J. Patokoski, R. L. Mauldin III, A.-P. Hyvärinen and H. Lihavainen, *Science*, 2010, **327**, 1243–1246.
20 I. Riipinen, J. Pierce, T. Yli-Juuti, T. Nieminen, S. Häkkinen, M. Ehn, H. Junninen, K. Lehtipalo, T. Petäjä and J. Slowik, *Atmos. Chem. Phys.*, 2011, **11**, 3865–3878.
21 I. Riipinen, T. Yli-Juuti, J. R. Pierce, T. Petäjä, D. R. Worsnop, M. Kulmala and N. M. Donahue, *Nat. Geosci.*, 2012, **5**, 453–458.
22 S. Okamoto and T. Okazoe, 1-hydroperfluorocycloalkanol-type cleaning agents for semiconductors substrates, *Japan Pat.*, JP2002220598 A, 2002.
23 R. Imasu, A. Suga and T. Matsuno, *J. Meteorol. Soc. Jpn. Ser. II*, 1995, **73**, 1123–1136.
24 Ø. Hodnebrog, M. Etminan, J. Fuglestvedt, G. Marston, G. Myhre, C. Nielsen, K. P. Shine and T. Wallington, *Rev. Geophys.*, 2013, **51**, 300–378.
25 W. J. Hehre, *Acc. Chem. Res.*, 1976, **9**, 399–406.
26 Y. Zhao and D. G. Truhlar, *Theor. Chem. Acc.*, 2008, **120**, 215–241.
27 Y. Zhao and D. G. Truhlar, *Acc. Chem. Res.*, 2008, **41**, 157–167.
28 Y. Zhao and D. G. Truhlar, *J. Chem. Phys.*, 2006, **125**, 194101.
29 A. McLean and G. Chandler, *J. Chem. Phys.*, 1980, **72**, 5639–5648.
30 R. Krishnan, J. S. Binkley, R. Seeger and J. A. Pople, *J. Chem. Phys.*, 1980, **72**, 650–654.
31 K. Guleria and R. Subramanian, *ACS Earth Space Chem.*, 2023, **7**, 947–959.
32 K. Guleria and R. Subramanian, *ACS Earth Space Chem.*, 2022, **6**, 1596–1611.
33 J. Pal and R. Subramanian, *Phys. Chem. Chem. Phys.*, 2019, **21**, 6525–6534.
34 P. Arathala and R. A. Musah, *ACS Earth Space Chem.*, 2021, **5**, 2878–2890.
35 P. Arathala and R. A. Musah, *ACS Earth Space Chem.*, 2021, **5**, 1498–1510.
36 C. Gonzalez and H. B. Schlegel, *J. Chem. Phys.*, 1989, **90**, 2154–2161.
37 C. Gonzalez and H. B. Schlegel, *J. Phys. Chem.*, 1990, **94**, 5523–5527.
38 R. Dennington, T. Keith, J. Millam and V. GaussView, *GaussView, Version*, Shawnee Mission, KS, 2009, **vol. 5**.
39 J. A. Pople, M. Head-Gordon and K. Raghavachari, *J. Chem. Phys.*, 1987, **87**, 5968–5975.
40 T. H. Dunning Jr, *J. Chem. Phys.*, 1989, **90**, 1007–1023.
41 S. Xu, J. Liang, S. Cao, R. He, G. Yin and Q.-D. Wang, *ACS Omega*, 2022, **7**, 8675–8685.
42 T. J. Lee and P. R. Taylor, *Int. J. Quantum Chem.*, 1989, **36**, 199–207.
43 J. C. Rienstra-Kiracofe, W. D. Allen and H. F. Schaefer, *J. Phys. Chem. A*, 2000, **104**, 9823–9840.
44 Y. Zhao and D. G. Truhlar, *Theor. Chem. Acc.*, 2008, **120**, 215–241.
45 K. Huber, *Molecular spectra and molecular structure: IV. Constants of diatomic molecules*, Springer Science & Business Media, 2013.
46 D. Van Der Spoel, E. Lindahl, B. Hess, G. Groenhof, A. E. Mark and H. J. Berendsen, *J. Comput. Chem.*, 2005, **26**, 1701–1718.
47 J. Wang, R. M. Wolf, J. W. Caldwell, P. A. Kollman and D. A. Case, *J. Comput. Chem.*, 2004, **25**, 1157–1174.
48 A. W. Sousa da Silva and W. F. Vranken, *BMC Res. Notes*, 2012, **5**, 367–374.
49 G. Bussi, D. Donadio and M. Parrinello, *J. Chem. Phys.*, 2007, **126**, 014101.
50 H. Kim, B. Fábián and G. Hummer, *J. Chem. Theory Comput.*, 2023, **19**, 8919–8929.
51 S. Grimme, J. Antony, S. Ehrlich and H. Krieg, *J. Chem. Phys.*, 2010, **132**, 154104.
52 B. Hess, H. Bekker, H. J. Berendsen and J. G. Fraaije, *J. Comput. Chem.*, 1997, **18**, 1463–1472.
53 E. R. Thornton, *J. Am. Chem. Soc.*, 1967, **89**, 2915–2927.
54 J. Zheng, J. L. Bao, R. Meana-Pañeda, S. Zhang, B. Lynch, J. Corchado, Y. Chuang, P. Fast, W. Hu and Y. Liu, *Poyrate-Version 2017-C,* University of Minnesota, Minneapolis, MN, 2017.
55 B. C. Garrett and D. G. Truhlar, *J. Chem. Phys.*, 1979, **70**, 1593–1598.
56 B. C. Garrett and D. G. Truhlar, *J. Am. Chem. Soc.*, 1979, **101**, 4534–4548.
57 B. C. Garrett, D. G. Truhlar, R. S. Grev and A. W. Magnuson, *J. Phys. Chem.*, 1980, **84**, 1730–1748.
58 D. G. Truhlar and A. Kuppermann, *J. Am. Chem. Soc.*, 1971, **93**, 1840–1851.
59 A. Fernandez-Ramos, B. A. Ellingson, B. C. Garrett and D. G. Truhlar, *Rev. Comput. Chem.*, 2007, **23**, 125.
60 D.-H. Lu, T. N. Truong, V. S. Melissas, G. C. Lynch, Y.-P. Liu, B. C. Garrett, R. Steckler, A. D. Isaacson, S. N. Rai and G. C. Hancock, *Comput. Phys. Commun.*, 1992, **71**, 235–262.
61 Y. P. Liu, G. C. Lynch, T. N. Truong, D. H. Lu, D. G. Truhlar and B. C. Garrett, *J. Am. Chem. Soc.*, 1993, **115**, 2408–2415.
62 L. Gui-Xia, G. Tao, C. Dong, L. Yue-Xun, Z. Yun-Guang and Z. Zheng-He, *Chin. Phys.*, 2006, **15**, 998.
63 Y. Shang, H. Ning, J. Shi, Y. Wu and S.-N. Luo, *J. Phys. Chem. A*, 2022, **126**, 825–833.
64 D. Singleton and R. Cvetanovic, *J. Am. Chem. Soc.*, 1976, **98**, 6812–6819.
65 V. H. Uc, I. García-Cruz, A. Hernandez-Laguna and A. Vivier-Bunge, *J. Phys. Chem. A*, 2000, **104**, 7847–7855.

66 A. Cruz-Torres and A. Galano, *J. Phys. Chem. A*, 2007, **111**, 1523–1529.
67 J. R. Alvarez-Idaboy, N. Mora-Diez, R. J. Boyd and A. Vivier-Bunge, *J. Am. Chem. Soc.*, 2001, **123**, 2018–2024.
68 K. Guleria and R. Subramanian, *Theor. Chem. Acc.*, 2022, **141**, 77.
69 W. Bradley, S. Wyatt, J. Wells, M. Henley and G. Graziano, *Int. J. Chem. Kinet.*, 2001, **33**, 108–117.
70 T. J. Wallington, P. Dagaut, R. Liu and M. J. Kurylo, *Int. J. Chem. Kinet.*, 1988, **20**, 541–547.
71 A. Hatipoğlu and Z. Çinar, *J. Mol. Struct. THEOCHEM*, 2003, **631**, 189–207.
72 I. Colmenar, P. Martin, B. Cabañas, S. Salgado, A. Tapia and I. Aranda, *Atmos. Chem. Phys.*, 2020, **20**, 699–720.
73 C. W. Spicer, E. G. Chapman, B. J. Finlayson-Pitts, R. A. Plastridge, J. M. Hubbe, J. D. Fast and C. M. Berkowitz, *Nature*, 1998, **394**, 353–356.
74 O. W. Wingenter, D. R. Blake, N. J. Blake, B. C. Sive, F. S. Rowland, E. Atlas and F. Flocke, *J. Geophys. Res.:Atmos.*, 1999, **104**, 21819–21828.
75 R. Hein, P. J. Crutzen and M. Heimann, *Global Biogeochem. Cycles*, 1997, **11**, 43–76.
76 R. Prinn, J. Huang, R. Weiss, D. Cunnold, P. Fraser, P. Simmonds, A. McCulloch, C. Harth, P. Salameh and S. O'doherty, *Science*, 2001, **292**, 1882–1888.
77 A. Hofzumahaus, F. Rohrer, K. Lu, B. Bohn, T. Brauers, C.-C. Chang, H. Fuchs, F. Holland, K. Kita and Y. Kondo, *Science*, 2009, **324**, 1702–1704.
78 K. Guleria, S. Tiwari, D. Barman, S. Daschakraborty and R. Subramanian, *Electron Density: Concepts, Computation and DFT Applications*, 2024, pp. 527–549.
79 S. Tiwari and R. Subramanian, *Theor. Chem. Acc.*, 2024, **143**, 1–15.
80 I. Bravo, A. Aranda, M. D. Hurley, G. Marston, D. R. Nutt, K. P. Shine, K. Smith and T. J. Wallington, *J. Geophys. Res.:Atmos.*, 2010, **115**, D24317.
81 B. Dimitriades, *J. Air Waste Manage. Assoc.*, 1999, **49**, 831–838.
82 A. Bouwman, *Water, Air, Soil Pollut.*, 2022, **141**, 349–382.
83 D. Granados Sánchez, G. López Ríos and M. Hernández García, *Rev. Chapingo Ser. Cienc. For. Ambiente.*, 2010, **16**, 187–206.
84 H. Huang, *Int. J. Environ. Stud.*, 1992, **41**, 267–275.
85 J. Tirado-Rives and W. L. Jorgensen, *J. Chem. Theory Comput.*, 2008, **4**, 297–306.
86 K. E. Riley, B. T. Op't Holt and K. M. Merz, *J. Chem. Theory Comput.*, 2007, **3**, 407–433.
87 C. Y. Go and K. C. Kim, *J. Phys. Chem. A*, 2024, 2245–2252.
88 J. Jang, K. H. Jung and K. C. Kim, *Sci. Rep.*, 2022, **12**, 7027.
89 B. Zhang, L. Chen, X. Li, Z. Guo, Y. Pu and N. Tang, *IEEE Trans. Dielectr. Electr. Insul.*, 2020, **27**, 1187–1194.
90 G. da Silva, J. W. Bozzelli, L. Liang and J. T. Farrell, *J. Phys. Chem. A*, 2009, **113**, 8923–8933.
91 J. Zádor, R. X. Fernandes, Y. Georgievskii, G. Meloni, C. A. Taatjes and J. A. Miller, *Proc. Combust. Inst.*, 2009, **32**, 271–277.
92 S. Wang, Q. Zhang, G. Wang, Y. Wei, W. Wang and Q. Wang, *Atmos. Environ.*, 2023, **304**, 119727.
93 X. Zhao, X. Shi, X. Ma, C. Zuo, H. Wang, F. Xu, Y. Sun and Q. Zhang, *Sci. Total Environ.*, 2020, **723**, 137987.
94 X. Shi, G. Huang, D. Yang, Q. Zhang, W. Zong, J. Cheng, X. Sui, F. Yuan and W. Wang, *Sci. Total Environ.*, 2021, **780**, 146422.
95 S. Wang, Q. Zhang, W. Wang and Q. Wang, *J. Environ. Manage.*, 2023, **347**, 119079.

